Report No.:	DOE/ DE-FG02-09ER64747-3
DOE Project No.:	DE-FG02-09ER64747 (SUNY Stony Brook); DE-FG02-09ER64748 (Princeton University); (KP1702030-54908) Pacific Northwest National Laboratory
Project Title:	**EFFECTS OF PORE STRUCTURE CHANGE AND MULTI-SCALE HETEROGENEITY ON CONTAMINANT TRANSPORT AND REACTION RATE UPSCALING**
Investigators:	W. Brent Lindquist (blindquist@notes.cc.sunysb.edu), Stony Brook University
	Keith W. Jones (jones@bnl.gov), Stony Brook University
	Wooyong Um (Wooyong.Um@pnl.gov), Pacific Northwest National Laboratory
	Mark Rockhold (Mark.Rockhold@pnl.gov), Pacific Northwest National Laboratory
	Catherine A. Peters (cap@princeton.edu), Princeton University
	Michael A. Celia (celia@princeton.edu), Princeton University
Report:	Final Report
Project Start Date:	May 15, 2009
Reporting Period:	May 15 2009 to Feb 15 2013
Sponsoring Office:	DOE Office of Science (SC-23, BER)

SUMMARY

This project addressed the scaling of geochemical reactions to core and field scales, and the interrelationship between reaction rates and flow in porous media. We targeted reactive transport problems relevant to the Hanford site − specifically the reaction of highly caustic, radioactive waste solutions with subsurface sediments, and the immobilization of ^{90}Sr and ^{129}I through mineral incorporation and passive flow blockage, respectively. We addressed the correlation of results for pore-scale fluid-soil interaction with field-scale fluid flow, with the specific goals of (i) predicting attenuation of radionuclide concentration; (ii) estimating changes in flow rates through changes of soil permeabilities; and (iii) estimating effective reaction rates. In supplemental work, we also simulated reactive transport systems relevant to geologic carbon sequestration. As a whole, this research generated a better understanding of reactive transport in porous media, and resulted in more accurate methods for reaction rate upscaling and improved prediction of permeability evolution. These scientific advancements will ultimately lead to better tools for management and remediation of DOE's legacy waste problems.

We established three key issues of reactive flow upscaling, and organized this project in three corresponding thrust areas.
1) **Reactive flow experiments**. The combination of mineral dissolution and precipitation alters pore network structure and the subsequent flow velocities, thereby creating a complex interaction between reaction and transport. To examine this phenomenon, we conducted controlled laboratory experimentation using reactive flow-through columns.
   ⇨ **Results and Key Findings**:
   Four reactive column experiments (S1, S3, S4, S5) have been completed in which simulated tank waste leachage (STWL) was reacted with pure quartz sand, with and without Aluminum. The STWL is a caustic solution that dissolves quartz. Because Al is a necessary element in the formation of secondary mineral precipitates (cancrinite), conducting experiments under conditions with and without Al allowed us to experimentally separate the conditions that lead to

1

quartz dissolution from the conditions that lead to quartz dissolution plus cancrinite precipitation. Consistent with our expectations, in the experiments without Al, there was a substantial reduction in volume of the solid matrix. With Al there was a net increase in the volume of the solid matrix. The rate and extent of reaction was found to increase with temperature. *These results demonstrate a successful effort to identify conditions that lead to increases and conditions that lead to decreases in solid matrix volume due to reactions of caustic tank wastes with quartz sands.* In addition, we have begun to work with slightly larger, intermediate-scale columns packed with Hanford natural sediments and quartz. Similar dissolution and precipitation were observed in these colums. The measurements are being interpreted with reactive transport modeling using STOMP; preliminary observations are reported here.

2) **Multi-Scale Imaging and Analysis**. Mineral dissolution and precipitation rates within a porous medium will be different in different pores due to natural heterogeneity and the heterogeneity that is created from the reactions themselves. We used a combination of X-ray computed microtomography, backscattered electron and energy dispersive X-ray spectroscopy combined with computational image analysis to quantify pore structure, mineral distribution, structure changes and fluid-air and fluid-grain interfaces.

⇨ **Results and Key Findings:**
Three of the columns from the reactive flow experiments at PNNL (S1, S3, S4) were imaged using 3D X-ray computed microtomography (XCMT) at BNL and analyzed using 3DMA-rock at SUNY Stony Brook. The imaging results support the mass balance findings reported by Dr. Um's group, regarding the substantial dissolution of quartz in column S1. An important observation is that of grain movement accompanying dissolution in the unconsolidated media. The resultant movement changes the anticipated findings for pore and throat size distributions. For column S3, with cancrinite precipitation accompanying quartz dissolution, the precitiation halts much of the grain movement and more systematic distributions are obtained. Column S4, which was sealed with caustic solution acted as a control sample to study reactive effects during periods when columns S1 and S3 were sealed between flow experiments. No significant changes are observed in S4 with time.

At Princeton, the imaging and analysis work focused on the effects of mineral precipitation and advancing our understanding of the impacts of these reactions on reactive transport in subsurface sediments. These findings are described in detail below, and have been published in L.E. Crandell, C.A. Peters, W. Um, K.W. Jones, W.B. Lindquist, 2012. "Changes in the pore network structure of Hanford sediment after reaction with caustic tank wastes." *Journal of Contaminant Hydrology* 131 (2012) 89–99.

3) **Multi-Scale Modeling and Up-Scaling**. Using an array of modeling approaches, we examined pore-scale variations in physical and mineralogical properties, flow velocities, and (for unsaturated conditions) wetting fluid/grain surface areas, and permeability evolution.

⇨ **Results and Key Findings:**
To predict the column permeability and estimate the impact of mineral precipitation, pore network models were informed using the pore and throat-size distributions from the imaging analyses. As a comparison, supplemental analyses were performed on Viking sandstone specimens from the Alberta sedimentary basin.

In another part of this study we sought to understand how carbonate rocks in contact with CO_2-rich brines change due to the precipitation or dissolution of fast-reacting minerals such as calcite and dolomite. Using a newly developed reactive-transport pore-network model we were able to identify the conditions that lead to significant permeability changes. These findings are presented below and are compiled in a publication that is under review: J.P. Nogues, J.P. Fitts, M.A. Celia,

C.A. Peters. "Permeability evolution due to dissolution and precipitation of carbonates using reactive transport modeling in pore networks", Submitted: *Water Resources Research*, 2013.

PUBLICATIONS DERIVED FROM THIS PROJECT

1. J. Kim, D. Kim and W.B. Lindquist. "A re-examination of throats." Submitted: *Water Resourc. Res.*, 2013.
2. L.E. Beckingham; C.A. Peters; W. Um; K.W. Jones; W.B. Lindquist. "2D and 3D imaging resolution trade-offs in quantifying pore throats for prediction of permeability", Submitted: *Adv. Water Resourc*., 2013.
3. J.P. Nogues, J.P. Fitts, M.A. Celia, C.A. Peters. "Permeability evolution due to dissolution and precipitation of carbonates using reactive transport modeling in pore networks", Submitted: *Water Resourc. Res*, 2013.
4. D. Kim and W.B. Lindquist. "Effects of network changes on pore-to-core up-scaled reaction rates", Submitted: *Water Resourc. Res*., 2013.
5. K.W. Jones, J. Wang, Y.-C. Chen, Q. Yuan, W.B. Lindquist, L.Beckinghaml, C.A. Peters, W. Um, L. Newman, T. Sabo-Attwood, R. Tappero. "Tomographic Investigations Relevant to the Rhizosphere," In: *Soil-Water-Root Processes: Advances in Tomography and Imaging.* Special Publication 61, S.H. Anderson and J.W. Hopmans, editors; SSSA, publisher, 2013.
6. G. Wang and W. Um. 2013. "Facilitated strontium transport by remobilization of strontium-containing secondary precipitates in Hanford Site subsurface", *J. Hazard. Mat.*, 248-249 (2013) 364–370.
7. G. Wang and W. Um. "Mineral dissolution and secondary precipitation on quartz sand in simulated Hanford Tank solutions affecting subsurface porosity", *J. Hydrol.,* 472-473 (2012) 159-168.
8. L.E. Crandell, C.A. Peters, W. Um, K.W. Jones, W.B. Lindquist. "Changes in the pore network structure of Hanford sediment after reaction with caustic tank wastes", *J. Contam. Hydrol.* 131 (2012) 89–99.
9. K.A. Chang and W.B. Lindquist. "A network model for the genesis and migration of gas phase", *Comput. Geosci.,* 17 (2012) 67−81.
10. D. Kim and W.B. Lindquist. "A semi-analytic model for the computation of imbibition through throats of polygonal cross section", *Water Resourc. Res.,* 48 (2012) W04529.
11. D. Kim and W.B. Lindquist. Dependence of pore-to-core up-scaled reaction rate on flow rate in porous media, *Trans. Porous Media*, 89 (2011) 459−473; republished in a special issue *ibid,* 94 (2012) 555−569.
12. Kim, D., C. A. Peters, and W. B. Lindquist. "Upscaling geochemical reaction rates accompanying acidic CO_2-saturated brine flow in sandstone aquifers", *Water Resour. Res.*, 47 (2011) W01505.
13. R. Cai, W.B. Lindquist, W. Um and K.W. Jones. "Tomographic analysis of reactive fluid induced pore structure changes in flow column experiments", *Adv. Water Resour*. (2009) 32:1396−1403.

PRESENTATIONS DERIVED FROM THIS PROJECT

14. J.W. Kim, W.B. Lindquist. "A Re-Examination of Throats", 5'th International Conference on Porous Media, Prague, May 21-24, 2013.
15. W. Um and G Wang. "Enhanced transport of Sr by mobile secondary precipitates", Presented in 9th Washington Hydrogeology Symposium, Tacoma, WA, April 22-25, 2013.
16. W.B. Lindquist. "Up-scaling Reaction Rates from Pore to Core Scale", Taiwan National University, Taipei, Taiwan, Jan. 21, 2013.
17. G. Wang, K.W. Jones, W. Um, M.L. Rockhold, L.E. Crandell, C. Peters, W.B. Lindquist. "Time-Dependent Measurements of Dissolution-Precipitation Reactions Caused by Caustic Waste Solutions at the Hanford Site Using Synchrotron Computed Microtomography", AGU Fall Meeting, San Francisco, CA, Dec. 3-7, 2012.
18. L.E. Crandell, C.A. Peters, W. Um, K.W. Jones, W.B. Lindquist, "2D imaging in a 3D world: Observing sub-grain scale variations and secondary mineral precipitates in reacted pore networks", Abstract H53G-1610 presented at Fall Meeting, AGU, San Francisco, CA, Dec. 3-7, 2012.

19. K. W. Jones, R. Tappero, J. Wang, Y-c. Chen, Q. Yuan, W. B. Lindquist, L. Crandell, C. A. Peters, W. Um, L. A. Newman, T. Sabo-Atwood, C. Moyer. "Tomographic Investigations of the Rhizosphere", ASA, CSSA, and SSSA International Annual Meetings, Cincinnati, OH, October 21-24, 2012.

20. W. B. Lindquist, "Capturing Heterogeneity and Bridging Scales in Reactive Flows", Flow and Transport in Permeable Media GRC, Les Diablerets, Switzerland, June 24-29, 2012.

21. J. P. Nogues, M. A. Celia, C. A. Peters. "Pore Network Model Development to Study Dissolution and Precipitation of Carbonates", XIX International Conference on Water Resources CMWR 2012, June 17-22, 2012.

22. W. B. Lindquist, "Upscaling Reaction Rates from Pore to Core Scale", International Conference on Flow and Transport in Porous Media, Poros, Greece, April 18-20, 2012.

23. G. Wang and W. Um. "Facilitated Contaminant Transport by Remobilization of Sr Containing Colloid-Sized Secondary Precipitates in Hanford Site", 243rd ACS National Meeting and Exposition, San Diego, CA, March 25-29, 2012.

24. L.E. Crandell, C.A. Peters, W. Um, W.B. Lindquist, "Intragranular Porosity in Hanford Sediment: Quantification and Implications for Radionuclide Trapping", 243rd ACS National Meeting and Exposition, San Diego, CA, March 25 - 29, 2012.

25. Lauren E. Crandell; Catherine A. Peters; Wooyong Um; Keith W. Jones; W B. Lindquist. "Intragranular porosity in Hanford sand grains after reaction with caustic tank wastes: Quantification and implications for reactive transport", Abstract H23C-1265 presented at Fall Meeting, AGU, San Francisco, CA, Dec. 5-9, 2011.

26. W B. Lindquist; D. Kim; C.A. Peters. "Dependence of Up-Scaled Reaction Rate on Flow Rate in Porous Media", Abstract GC51A-0939 presented at Fall Meeting, AGU, San Francisco, CA, Dec. 5-9, 2011.

27. J. P. Nogues, C. A. Peters, J. P. Fitts, M. A. Celia (2011), Investigation of dissolution and precipitation of carbonate rocks using reactive transport modeling in pore networks, Abstract GC51A-0940 presented at 2011 Fall Meeting, AGU, San Francisco, CA, 5-9 Dec.

28. C. A. Peters, L. E. Crandell, W. Um, K. W. Jones, W. B. Lindquist. "The 2D versus 3D imaging trade-off: The impact of over- or under-estimating small throats for simulating permeability in porous media", Abstract H53N-02 presented at 2011 Fall Meeting, AGU, San Francisco, CA, 5-9 Dec. 5-9, 2011.

29. L. Crandell, C. A. Peters, W. Um, K. Jones, B. Lindquist. "Changes in the pore network structure of Hanford sand after reaction with caustic tank wastes." Poster presentation at Global Sustainability and Environmental Engineering: AEESP 2011 Conference, Univ. of South FL, July 2011, Tampa, FL.

30. G. Wang and W. Um . "Radionuclide Immobilization and Flow Path Modifications by Dissolution and Secondary Precipitates", 8th Washington Hydrogeology Symposium, Tacoma, WA, April 26-28, 2011.

31. W. B. Lindquist, D. Kim, K.W. Jones, C.A. Peters, M. Celia, W. Um, M. Rockhold. "Up-Scaling Reaction Rates from Pore-to-Core Scale via Reactive Network Flow Modeling", *DOE-SBR* 6th Annual PI Meeting, Washington, DC, April 26-28, 2011.

32. W.B. Lindquist, R. Cai, K.W. Jones, W. Um. "Tomographic Analysis of Reactive Flow Induced Pore Structure Changes in Column Experiments", CVIII International Conference on Water Resources, June 21-24, Barcelona, 2010.

33. L.E. Crandell, C.A. Peters, W. Um, W.B. Lindquist. "Sub-grain scale mineralogy of Hanford sand after reaction with caustic tank wastes", Abstract H41D-1108 2010 Fall Meeting, AGU, San Francisco, CA, 2010.

34. W. B. Lindquist. R. Cai, K.W. Jones, W.Um. "Tomographic Analysis of Reactive Flow Induced Pore Structure Changes in Column Experiments", International Conference on Non-linearities and Upscaling in Porous Media, Stuttgart, Germany, July. 2009.

AWARDS related to this work

Outstanding Presentation Award, ACS National Meeting March 2012, for "Intragranular porosity in Hanford sediment", with Lauren Crandell.

2011 Outstanding Student Paper Award to PhD student Juan Nogues, 2011 AGU Fall Meeting

2011 Poster Award, first author PhD student Lauren Crandell, AEESP Education and Research Conference

DETAILED REPORT

1. Reactive Flow Experiments at PNNL

Mineral dissolution and precipitation reactions can alter pore structure and flow behavior, thereby creating more complex interactions between reaction and transport processes in the subsurface. To examine this phenomenon and to quantify impacts, we conducted controlled laboratory experiments at PNNL with pure quartz sand and Hanford sediment-packed columns. We report here the experimental results.

1.1 Summary of experiments

Three mini columns, called "S1, S3, and S4", with 2.1 mm internal-diameter and 10 cm length were prepared by packing them with pure quartz sand (200-300 µm diameter) that had been acid washed. After packing, the columns were sent to BNL for pre-experiment X-ray imaging (XCMT) at the synchrotron light source. After initial scanning, the columns were returned to PNNL and synthetic tank waste leachate (STWL) with and without Aluminum was introduced into different columns (no Al in S1 column and with Al in S3 and S4 columns) under saturated conditions and at elevated temperatures (45°C and 88°C using water bath). The compositions of the STWL (pH=13.3) and columns in which these solutions were used are shown in Table 1.1. Different pore structure changes are expected since Al is a necessary element to form the secondary mineral precipitates dominated by feldspathoid, sodalite or cancrinite. STWL without Al can only result in quartz dissolution. Column S4 was used as a no-flow column to determine the static effects of dissolution and precipitation by STWL containing Al. One additional flow-through mini-column experiment, called "S5", was also performed. The S5 column had different dimensions than the other columns, with 4.6 mm internal-diameter and 5-cm length. This column was prepared using the same quartz sand material. Column S5 was treated with STWL containing Al, similar to column S3. A similar dissolution and precipitation reaction is expected to occur in the column S5. The larger scale was used for the purposes of testing an XCMT system at PNNL and comparing with the results from column S3.

Table 1.1. Composition of STWL without and with Al and corresponding columns

Elements	Column designations and STWL compositions (M)	
	S1	S3, S4, S5
Na^+	2.2	2.2
OH^-	1	1
NO_3^-	1.2	1.275
Sr^{2+}	1.0E−5	1.0E−5
Al^{3+}	-	0.025

Three separated KLOEHN V6 syringe pumps were used to produce a steady flow of STWL solution to each column. The pumps offered a constant flow instead of constant pressure. As long as the pore space inside columns was not totally clogged, the syringe pumps maintain constant flow rates. The entire column experiments were performed under two temperature steps (45°C and 89°C) and at two flow rates. The reaction temperature was initially set to 45°C, and the flow rate for all the columns was initially set to a constant value of 0.07 mL/h, resulting in 13.1, 14.9, and 4.8 PV (pore volume)/day for columns S1, S3, and S5, respectively. This flow rate (0.07 mL/h), i.e., 0.24-1.3 m/day in terms of the true flow velocity in the packed columns, was chosen based on the general infiltration rate (2-3 cm/h or ~0.6 m/day) in soils, which is similar to the gravel sand dominated sediment at Hanford site. After 155-, 147-, and 199-day reactions of the columns S1, S3, and S5, respectively, the flow rate was manually decreased to 0.023 mL/h (correspondingly 4.3, 4.9, and 1.6 PV/day for S1, S3, and S5, respectively). Furthermore, after 7 days of column operation under the reduced flow rate at 45°C, the reaction temperature was increased to 89°C to further accelerate chemical reactions (dissolution and secondary precipitation) till the end of entire experiment. The

flow rates in three columns during the experiments were monitored to be constant, except when the manual reductions were imposed. The experimental setup is shown in Figure 1.1.

After reactions had been allowed to proceed for a certain amount of time, flow was stopped and the columns were sealed and shipped back to BNL for XCMT analysis. During the course of these column experiments (about 625 days for the total process), columns S1, S3, and S5 were disconnected from the pump five times and were shipped to BNL (together with column S4). The XCMT imaging time-points ($t_0 - t_6$) are shown in Figure 1.2.

Fig 1.1. Experimental setup for mineral dissolution and secondary precipitation saturated flow-through column experiments under high alkaline condition using PEEK columns, syringe pumps, and water bath (45°C or 89°C).

In addition to mini-column experiments, for upsacling purpose and also testing the dissolution and precipitation phenomenon in natural sediments, three intermediate size PEEK columns (ID 19.1 mm with 91 mm length), called "Hanford C1, Hanford C2, and Quartz C" were packed with either Hanford coarse sand (1−2 mm size fraction) or pure quartz sand (200-300 µm diameter). Similar to the mini-column experiment procedure, the same simulant tank waste leachate (STWL) with and without aluminum was introduced into different columns (no Al in Hanford C1 column and with Al in Hanford C2 and Quartz C columns) under saturated conditions at 89°C. The entire experiment flow rate was 0.18 mL/h (0.5 PV/day). XCMT imaging was performed at three time-points during the entire test (299 day flow-through) using PNNL XCMT system (see figure 1.2).
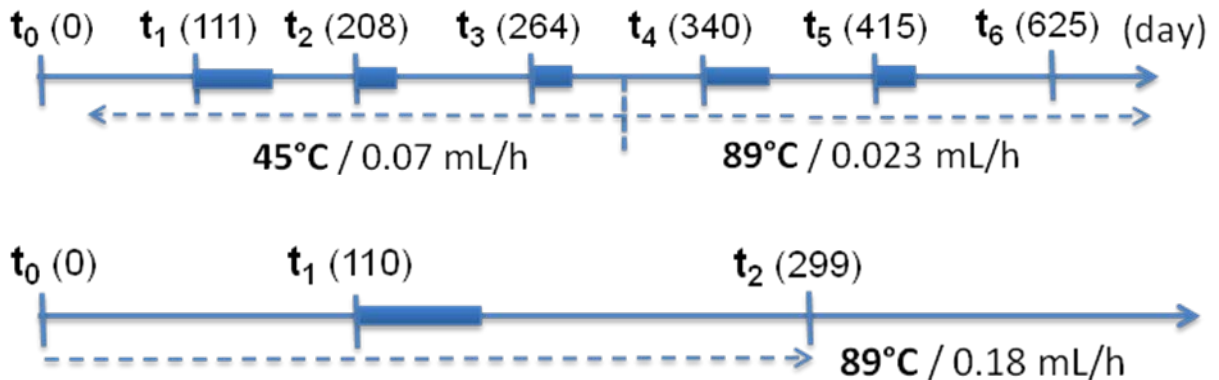
Figure 1.2. Column reaction and imaging history for mini-column S1, S3, S4, and S5 (upper plot), as well as for intermediate size columns of Hanford C1, Hanford C2,and Quartz C (lower plot); The letters t_0 to t_6 indicates the X-ray imaging collection times.

1.2 Results

Column Experiments: The measured concentrations of Si and Al in the effluents of columns S1, S3, and S5, respectively, are shown in Figure 1.3. No significant pH changes were observed between

input and effluent solutions (pH = 13.3) in all three columns. Generally, the observed Al and/or Si concentrations in all three columns (S1, S3, and S5) at 45°C were quite stable for a long time period until the flow rate was reset to 0.023 mL/h, resulting in concentration plateaus for both Al and Si at 45°C under constant flow rates. The effluent Al concentrations at this low temperature stage were quite similar to the input concentration of Al in the STWL+Al solution. The difference of Al concentration between input and output through both columns S3 and S5 was within ±5%, which is within the general laboratory equipment analysis error ranges. To increase the effect of Al consumption, the flow rate was reduced from the initial 0.07 mL/h to 0.023 mL/h and the temperature was increased to 89°C. The temperature increase to 89°C dramatically enhanced both dissolution and precipitation reactions, in which Si and Al effluent concentrations increased and decreased in columns S1 and S5, respectively. Column S3 also showed concentration changes in both Si and Al in a similar pattern. Different reaction extents between columns S3 and S5 may be attributable to differences in the quartz sand mass (reactant) packed inside the two columns. In column S3 after the Si peak concentration resulting from the temperature increase at 154 days of contact, the effluent Si concentration slowly decreased again from its concentration peak value. Meanwhile, the abrupt decrease in effluent Al concentration in column S3 when the temperature was increased at 154 days was correspondingly followed by a slow increase again. This phenomenon can be explained by the coverage effect of neo-formed (under higher temperature) nitrate-cancrinite on quartz sand grain surfaces which reduced the reactive surface sites, leading to a decreased dissolution of quartz and thus a reduced effluent Si concentrations as well. Correspondingly, a slight increase of effluent Al concentration was observed to reach the initial Al concentration again due to reduced consumption because the dissolved Si concentration decreased. In column S5, this transient quartz surface coverage phase was much less obvious than that found in column S3, which again could be explained by more quartz sand packed in column S5. Theoretically, a similar transient pattern can occur during the lower temperature test period, but the surface coverage effect from the neo-formed precipitate is considered negligible because of the much lower nitrate-cancrinite precipitation rate compared to that at 89°C. This transient surface coverage effect could be confirmed by the no-decreasing effluent Si concentration in column S1 in which no secondary mineral precipitate was formed because of no Al present in the STWL. This surface area coverage due to precipitation is directly demonstrated by SEM images. Further studies are needed to elucidate the dependence of the Si dissolution rates on the surface coverage by neo-precipitates, especially for estimating long-term dissolution and precipitation rates of natural soil and sediments at a field scale. No significant changes in Na concentrations were observed in any of the columns because of the relatively high initial Na concentration in the STWL compared to other elements.
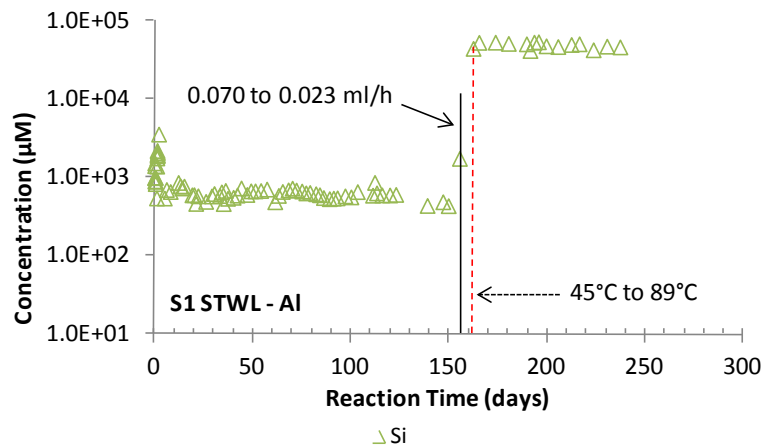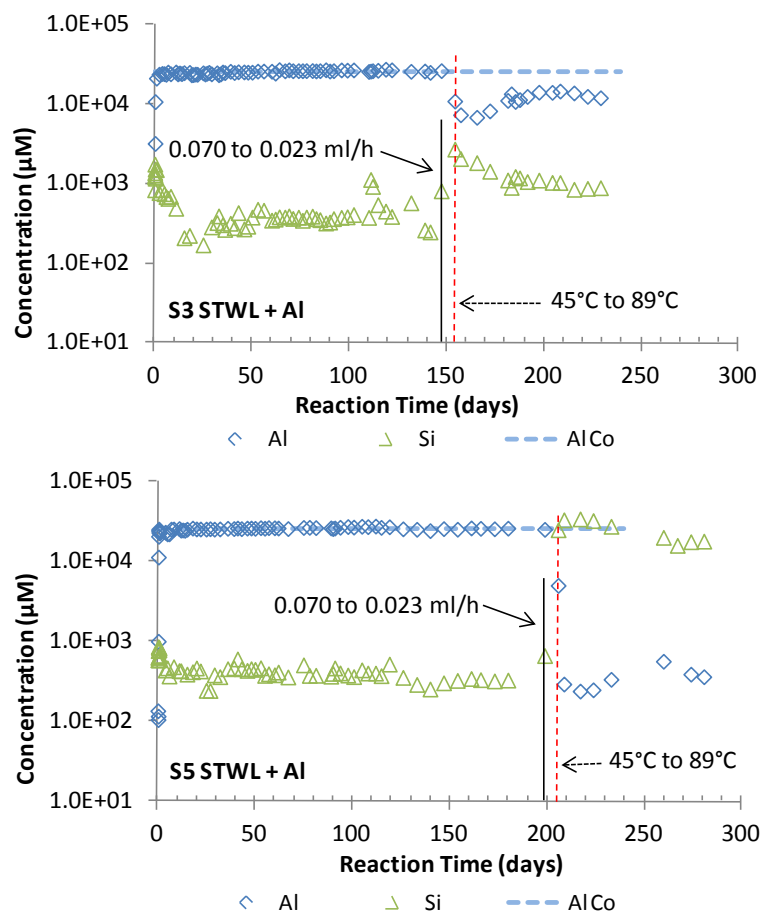
Figure 1.3. Measured effluent concentrations of Si and Al concentrations in the column experiments S1, S3 and S5; "STWL+ Al or STWL– Al" represent STWL solution with or without Al, respectively. The blue dashed lines denote the initial concentrations of Al (C_0 for Al) in STWL. The green triangle and blue diamond symbols indicate measured effluent Si and Al, respectively. The significant chemical concentrations change in the graphs resulted from flow rate and temperature being manually changed.

From mass balance, based on the measured input and effluent Si and Al concentrations and the effluent volume, either dissolved quartz or precipitated secondary mineral volume can be estimated. Table 1.2 shows the calculated solid volume and porosity changes inside columns at the end of tests due to dissolution and precipitation. Based on the measured Si concentration and effluent volume, about 23.8% volume of the initially packed quartz sand was removed by dissolution in column S1 after 237 days of reaction. For columns S3 and S5, both quartz dissolution and nitrate-cancrinite precipitation occurred synchronously during the entire testing period, so the final solid volume change after 229 (in column S3) to 280 (in column S5) days of reaction (compared to the initially packed solid volume) in each column was an increase of 13.2% and 5.9% for column S3 and S5, respectively. The negative volume change of quartz sand in column S1 confirms that only dissolution occurred in this column because the STWL-Al was used. However, the net positive volume change of columns S3 and S5 indicated that more volume of solid was created by secondary precipitation even if dissolution of quartz occurred. The net increase in the solid-phase volume could block the pores and affect permeability, flow rates, flow pathway, and other associated mass transfer processes inside the columns. Comparing to S1 column's initial porosity (pre-reaction) of 0.37, the porosity in the column matrix after reaction increased by 40.3% to 0.52. In columns S3 and S5,

the net change of dissolution and precipitation reactions at 89°C resulted in a decrease in porosity because the precipitation created more solid volume via solid-phase precipitation compared to the increase in porosity caused by quartz dissolution. The final porosity decreased by 26.5% and 8.4% in columns S3 and S5, respectively. Thus, the porosity changed from the initial 0.33 to 0.24 and from the initial 0.42 to 0.39 for the S3 and S5 columns, respectively.

Table 1.2. Solid volume and porosity changes inside columns at the end of experiment tests

Columns	S1	S3	S5
Volume change (%) of quartz sand to the initial packed sand volume based on the total eluted Si concentrations in the effluents	-23.8%	-1.5%	-4.2%
Volume change (%) of quartz sand portion only participating in precipitation to the initially packed sand volume based on the total eluted Al concentrations in the effluents	NA	-7.0%	-4.9%
Total volume change (%) of quartz sand to the initially packed sand volume	-23.8%	-8.5%	-9.1%
Percentage of nitrate-cancrinite volume created to the initially packed sand volume	NA	+21.7%	+15 %
Final volume change (%) of solid to the initially packed sand volume	-23.8%	+13.2%	+5.9%
Initial packed column porosity calculated [-]	0.37	0.33	0.42
Final column porosity calculated after STWL flow-through [-]	0.52	0.24	0.39
Final porosity change (%) after entire experiment	+40.3%	-26.5%	-8.4%

* Density of quartz sand: 2.65 g/cm^3; density value of 2.45 g/cm^3 was used for nitrate-cancrinite (Bickmore et al., 2001). The molecular weight (1,022 g/mol) of nitrate-cancrinite was calculated based on the chemical formula of $Na_8Si_6Al_6O_{24}(NO_3)_2$. Silica dissolution: $SiO_{2\,(quartz)} + 2OH^- = H_2SiO_4^{2-}$; precipitation: $6Al(OH)_4^- + 6H_2SiO_4^{2-} + 8Na^+ + 2NO_3^- = Na_6Si_6Al_6O_{24}\cdot2NaNO_3 + 12OH^- + 12H_2O$;

Calculated dissolution rates (on average) in column S1 (8.33E-12 mol/cm^2/s at 89°C, and 2.27E-13 mol/cm^2/s at 45°C) were about 3 times higher than those from column S3 (2.81E-12 mol/cm^2/s at 89°C, and 1.41E-13 mol/cm^2/s at 45°C) and column S5 (3.32E-12 mol/cm^2/s at 89°C and 1.21E-13 mol/cm^2/s at 45°C), indicating the difference between pure dissolution (S1) and dissolution/precipitation processes (S3 and S5). The lower dissolution rate values in columns S3 and S5 could result from the reacted surface effect due to precipitation. The determined rate in this study agrees reasonably well with literature (Dove & Rimstidt, 1994; Bickmore et al., 2006). The average "pseudo" precipitation rate was only determined for columns S3 (2.39 E-13 mol/cm^2/s) and S5 (2.28 E-13 mol/cm^2/s) at the 89°C test stage. We call it "pseudo" precipitation rate because the newly generated surface area, resulting from the neo-formed nitrate-cancrinite secondary precipitates which were attached on the quartz sand surface and also available for accepting further precipitation, was not taken into account in the rate estimation. The calculation was based on the initial grain surface of the packed sand.

Figure 1.4 shows the measured concentrations of Si and Al in the effluent of the intermediate columns Hanford C1 (STWL– Al), Hanford C2 (STWL+ Al), and Quartz C (STWL+ Al) at 89°C, respectively. No significant pH changes were observed between input and effluent solutions (pH = 13.3) in all three columns. The observed Si concentrations in Quartz C column were quite stable, while a decreasing trend was observed in both Hanford C1 and C2 columns. Interestingly, after the initial 10 pore volumes, no significant difference in Si concentration was observed between Hanford C1 and C2 columns that was flowed through with STWL−Al and STWL+Al, respectively. This is consistent with the observed Al concentration data. Despite two different input STWL solutions (with or without Al), the effluent Al in all three columns were quite similar with very low detected Al concentrations (i.e., C/C_o = ~0.01), which indicates that most of the input Al was consumed in the formation of secondary precipitate immediately at early stage. In the case of Hanford C1 column, in which STWL-Al was used, similar Al concentrations in the effluents were observed compared to the other two columns. This could be explained by Al release from the natural Al–containing minerals such as clays from the packed natural Hanford sediments. Overall, it implies that Al element in the

input STWL was almost totally consumed during the precipitation reaction inside the columns. Figure 1.5 shows the observed precipitates in the Quartz C and Hanford C2 column after 299 days of flow-through reaction at 89°C.
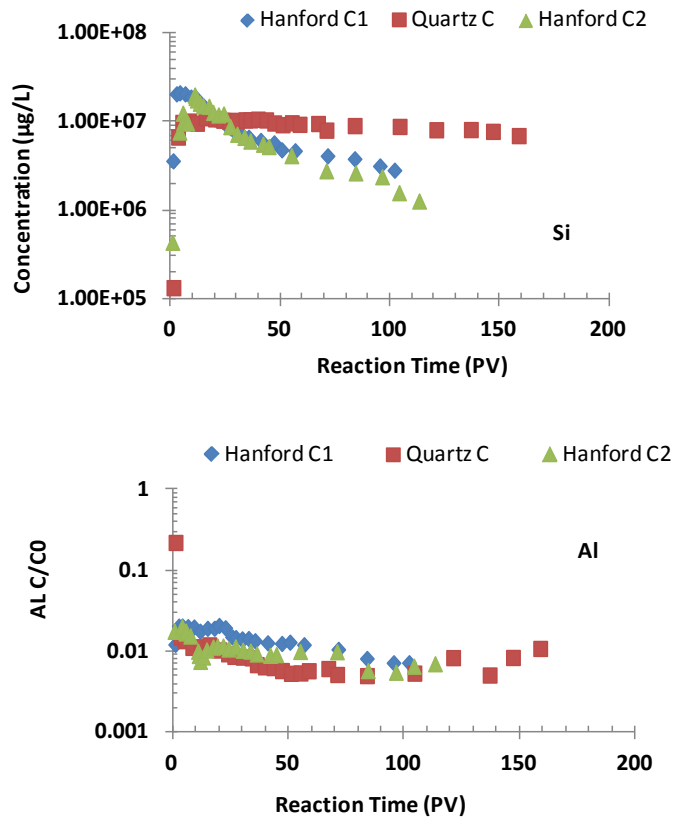

Figure 1.4. Measured effluent concentrations of Si and Al concentrations in the intermediate column experiments Hanford C1 (STWL– Al), Hanford C2 (STWL+ Al), and Quartz C (STWL+ Al) at 89°C.
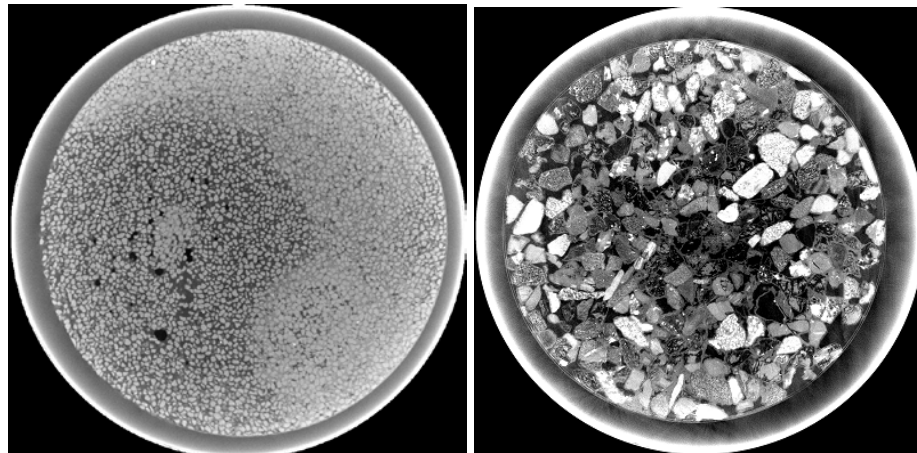

Figure 1.5. Observed precipitates in the Quartz C (left) and Hanford C2 (right) column after 299 day flow-through reaction at 89°C.

Intermediate-scale column and modeling results

A large, more realistic, range of grain sizes can be accommodated in the larger columns, relative to the small PEEK columns. Although larger volumes of interrogation generally result in lower spatial resolution for XMT imaging, pre- and post-reaction imaging for these intermediate columns was performed at PNNL using an XMT system housed in the Environmental Molecular Sciences Laboratory (EMSL). Figure 1.6 shows a slice from one of the experiments performed using the Hanford C2 sediment. The red box is the approximate area of a region of interest (ROI) that will be discussed in more detail.
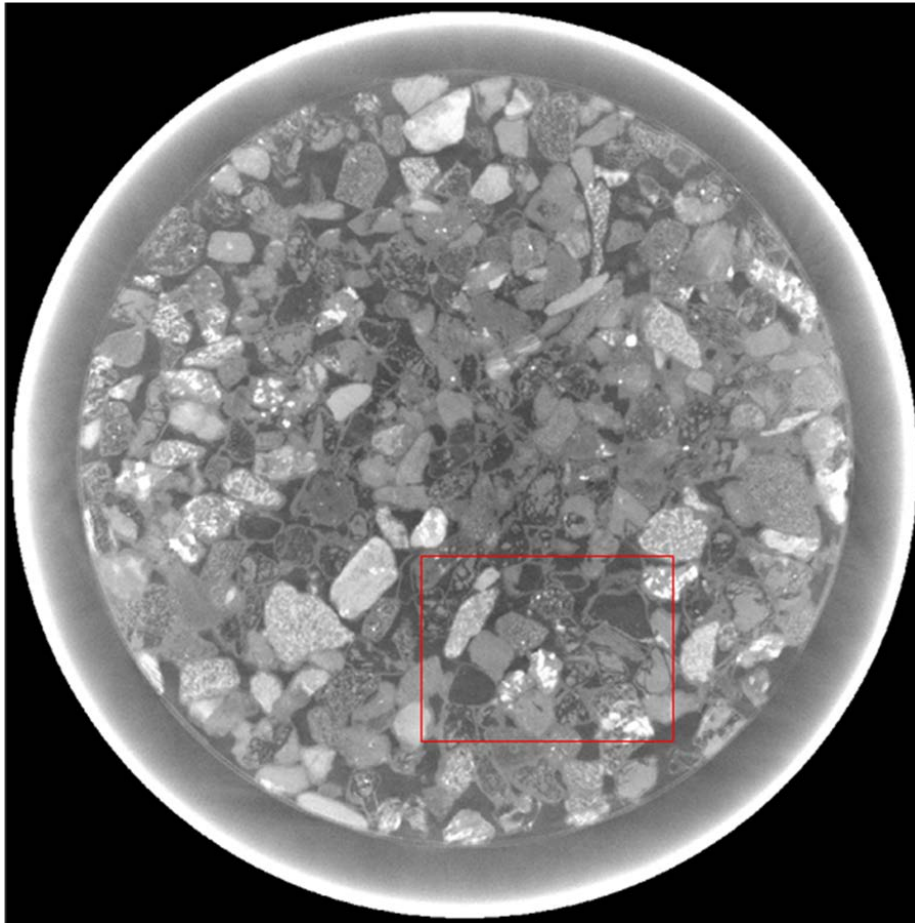
Figure 1.6. XMT image of a cross section through an intermediate-scale column packed with heterogeneous Hanford sediment (post reaction). The red box indicates a region of interest (ROI) shown in more detail Fig. 1.7.
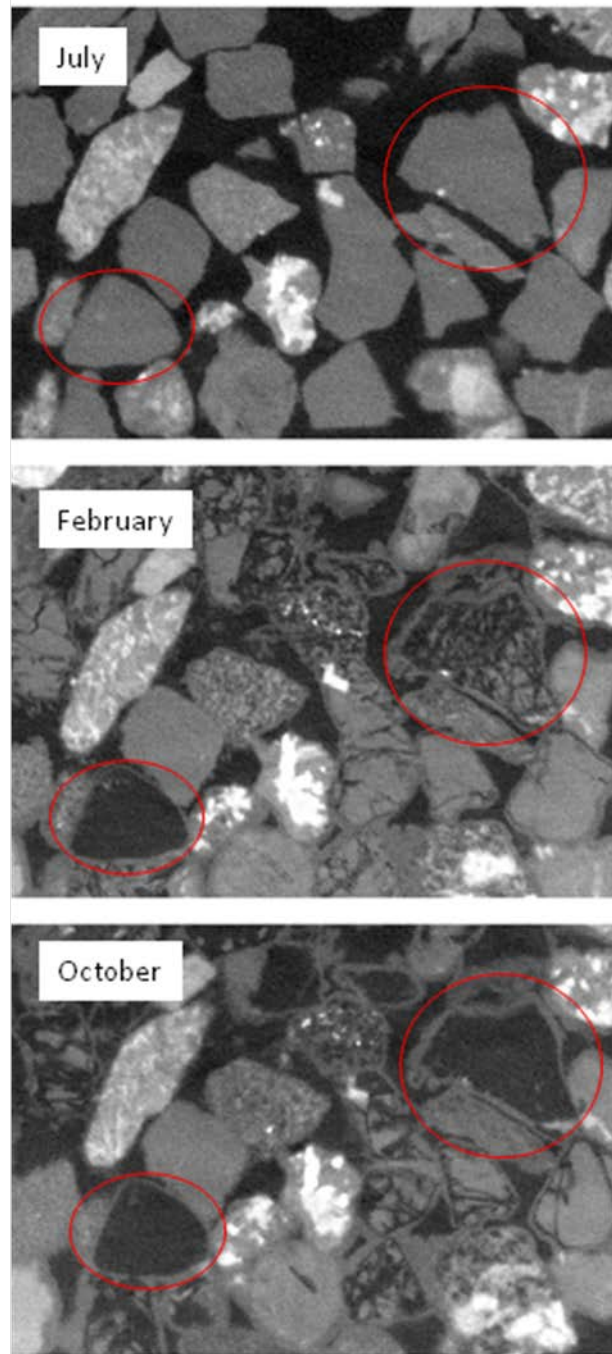
Figure 1.7. Images representing the ROI shown in Figure 1.6. The July image (top) represents the sediment prior to reaction. The February (middle) and October (bottom) images represent post-reaction sediments. The red ellipses illustrate regions that show apparent grain disappearance, or at least changes in the relative x-ray adsorption that give rise to the impression that grains are dissolving from the inside-out.

The XMT data obtained from the EMSL system for the Hanford sediments exhibit some interesting features. Specifically, some grains that initially appeared to be very similar to many others in the pre-reaction images seem to almost completely disappear after reaction, except for a thin rind of material around the area that was originally the edge of some of the grains. Visually, this gives the impression that some of the grains were dissolving from the inside-out which is counterintuitive, unless these grains contained micro-fractures that provided conduits for mass exchange. The other grains, which initially appeared to be similar, show no obvious changes in size or structure.

Pre- and post-reaction images were analyzed using custom software to obtain segmented results (Figure 1.8). Initial analyses were performed using simple binary segmentation with thresholds determined from measured porosity and un-reacted image results. Preliminary pore networks were constructed using the maximal ball algorithm (Dong and Blunt, 2009), which is an alternative to the medial axis method used in 3DMA-Rock. Figure 1.9 shows one example of such a pore network.
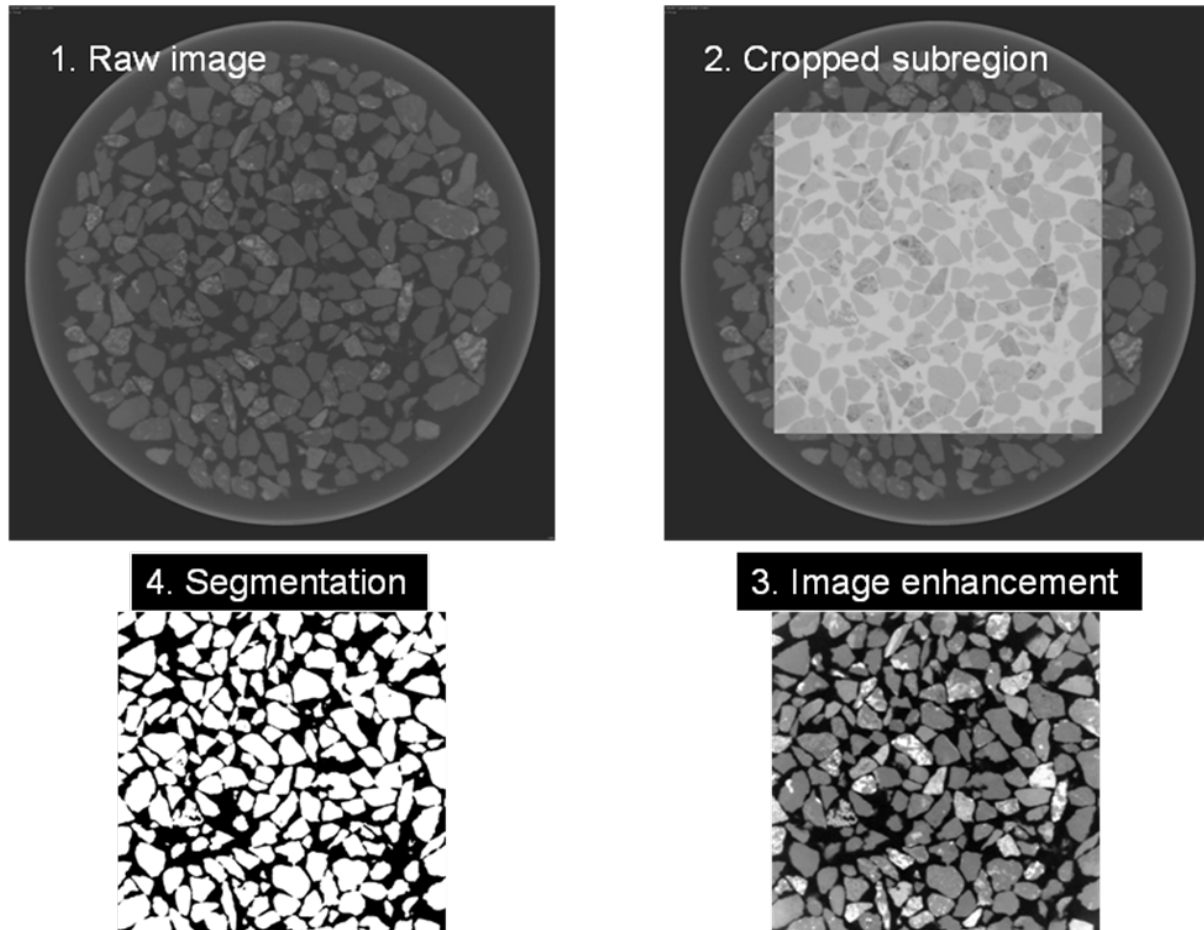
Figure 1.8. Image analysis steps for intermediate-scale column experiments.
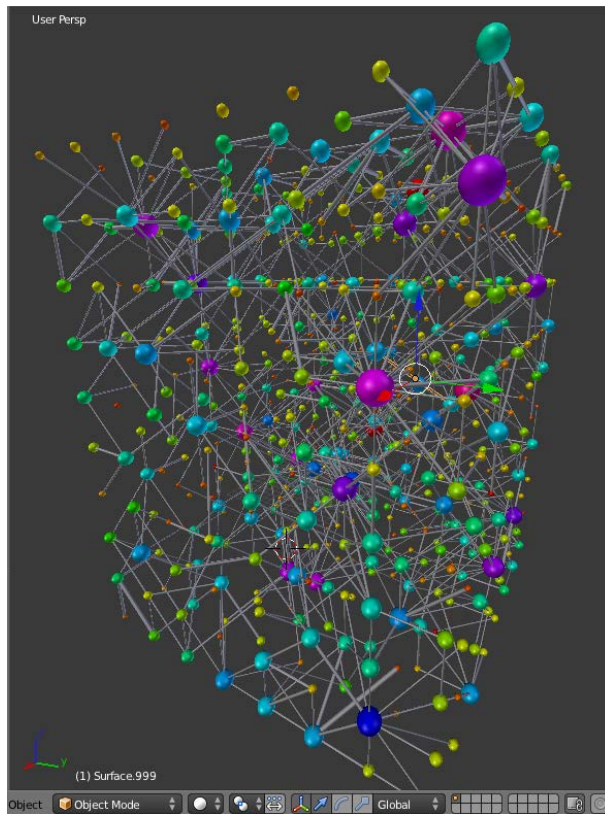
Figure 1.9. Example of pore network generated from pore body and throat size distributions obtained from XMT data.

An unstructured network flow solver was also developed for variably-saturated (quasi-static) flow conditions. Our intent was to use this solver in conjunction with the pore network information obtained from XMT imaging to address questions of upscaling mass transfer and reaction rates. This work is ongoing and differs somewhat from the pore network modeling efforts by the other groups in that it addresses transport and reaction under variably saturated flow conditions that occur in the vadose zone.

Reactive transport modeling of the intermediate-scale column experiments with SWTL in Hanford sediments was performed using the STOMP simulator. Fifteen aqueous species were considered: $Al(OH)_3$, Al^{3+}, Ca^{2+}, H^+, $H_2SiO_4^{2-}$, $HNO_3(aq)$, K^+, NO_3^-, Na^+, $NaOH(aq)$, OH^-, $SiO_2(aq)$, $Sr(NO_3)_2(aq)$, Sr^{2+}, and bromide tracer. Seven solid species were considered: Anorthite, cancrinite, gibbsite, K-feldspa, muscovite, quarts, tobermorite-11A. Equilibrium constants (logK) were taken from the thermo.minteq and datacom.dbs (CRUNCH) data bases. Kinetic TST formulations were used for mineral reactions. Simulated porosity reductions (Figure 1.10) are consistent with experimental results, showing that the bulk of the porosity reduction at the column inlet and with progressively less porosity reduction with distance from the inlet. In these simulations the porosity reduction is due primarily to precipitation of cancrinite.
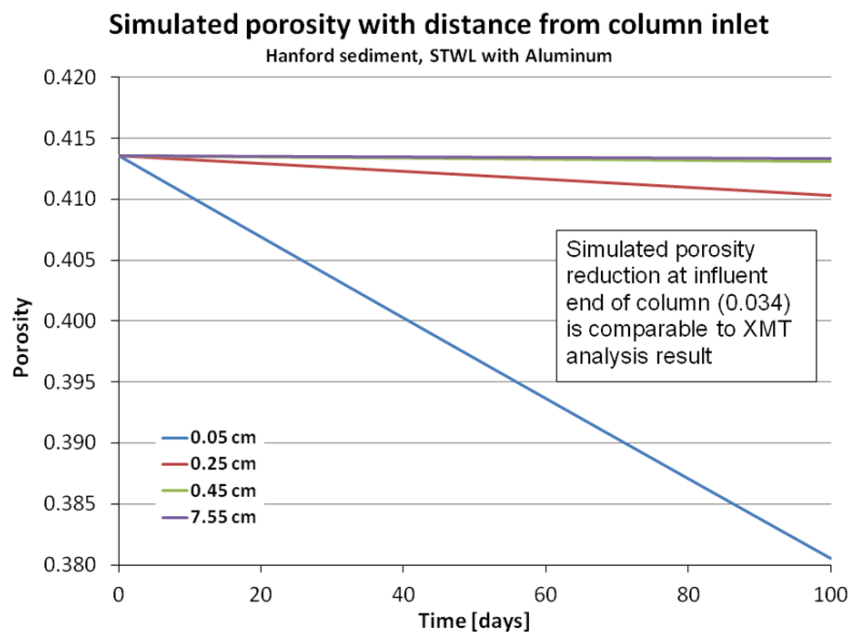
Figure 1.10. Simulated porosity variation with time and distance from column inlet for Hanford sediment and SWTL with aluminum.
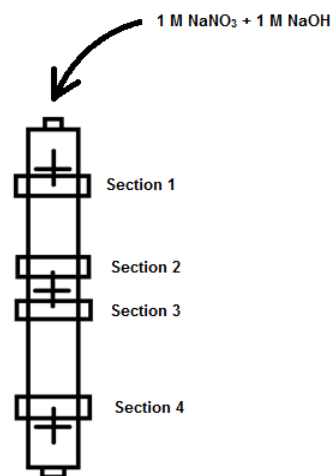
2. Multi-Scale Imaging and Analysis

### 2.1 3D X-ray computed micro tomographic (XCMT) image analysis

At Brookhaven, 3D X-ray computed micro tomographic (XCMT) imaging was done on four sections (Sections 1 - 4) of the columns S1, S3, S4 and S5. The location of the four sections are sketched in Figure 2.1. This was done before synthetic tank waste leachate (STWL) flow (R0, R1), and after each of five flow column "runs" (R2 – R6). The XCMT image voxel size was 4 μm. The images from S1 have been analyzed to see pore structure changes by STWL reactive flows using the software package 3DMA-Rock. The analyzed image volumes were typically $\pi \times 1.05^2 \times 2.4$ mm³ for S1, S3 and

S4.The diameter of column S5 exceeded the field of view of the XCMT imaging at 4 μm resolution and the images obtained were poorly resolved. We therefore report results only on columns S1, S3 and S4.

As mentioned in the first progress report, errors in the images such as ring artifacts and vertical dislocations in sinograms were carefully fixed and XCMT images allowing for micro-scale analyses were reconstructed.

Figure 2.1. Imaged four sections along column

Column S1 (sections 1 and 2), S3 (sections 1 – 4) and S4 (sections 1 – 4) were analyzed using the 3DMA-Rock software. Air bubbles were detected in S1 as shown in Figure 2.2, an image from
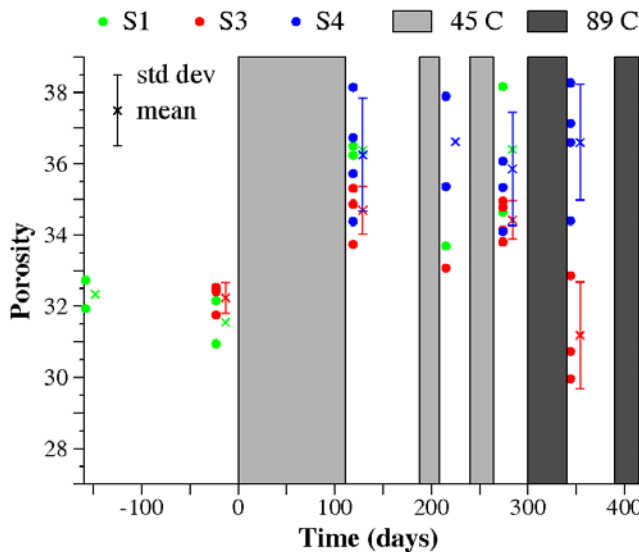
15
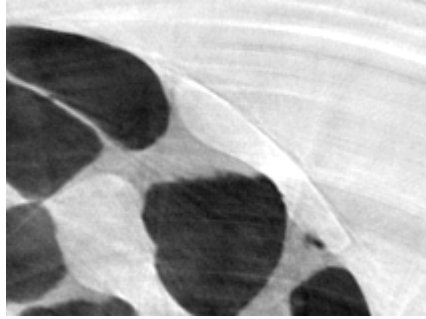
Figure 2.2. Air bubbles shown by XCMT image in Section 2 of S1. One bubble is present between the column wall and a sand grain and another bubble is among grains.

Section 2. The volume of detected air bubbles was approximately 10% of the total pore volume. Such bubbles were not detected in column S3 (column S4 was a sealed, no flow, column).

Figs. A1, A2 and A3 in Appendix A show the pore structure changes observed in segmented sample slices from columns S1, S3 and S4. The images on the same column/section had to be registered (translation and rotation) with respect to each other. Registration was performed on the segmented images. Registration was easiest for column 4, the control sealed column, although, as can be seen in Fig. A3 (compare image R6 with the earlier images) there is evidence of some limited sand grain movement. Registration for column S1, which exhibited only dissolution was the most difficult. The loss of 9-10% quartz volume resulted more significant grain movement. The combination of dissolution and precipitation in column S3 tended to lessen grain movement. However cancrinite precipitation resulted in grains taking on a "rougher" shape (R5 and R6 images in Fig. A2).

Figure 2.3. Porosity change as a function of time for all column/sections analyzed. Time 0 corresponds to the start of the first injection of STWL. The STWL flow periods occurred during the shaded time periods. Except for a baseline imaging (prior to STWL injection) XCMT imaging took place shortly after each flow column run. During the remainder of the time period, each column was sealed. The porosity of each section analyzed appears as a colored circle. The mean and, where appropriate, standard deviation of the porosity for each column is also given (offset slightly to the right of the data points).

The porosity changes observed from the XCMT images are shown in Figure 2.3. The STWL flow periods occurred during the shaded time periods. There were 3 periods of flow at 45 °C, and 2 periods at 89 °C. Except for a baseline imaging (prior to STWL injection) XCMT imaging took place shortly after each flow column run. During the remainder of the time period, each column was sealed.

Column S4 was filled with STWL initially, but was then sealed and never subjected to subsequent STWL flow. It therefore acted as a control to capture the reactive effects of sealing a column between one flow period and the next. Fig. 2.4 displays the porosity observed in each of the 4 sections of column S4. Time is suppressed in the plot; for each section, the porosity observations are relatively tightly clustered, indicating our ability to repeat porosity observations over time. For each section, the standard deviation of observed porosity varied between 0.17% and 0.64%. Averaging porosities over all sections and all time for column S4 gives a porosity of $36.3 \pm 1.5\%$.

16
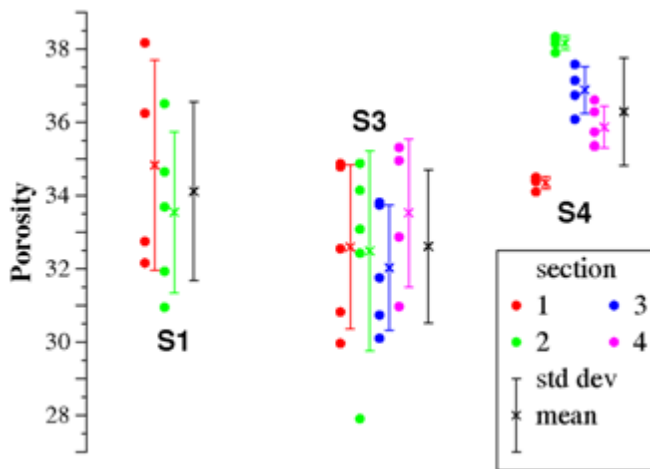
Figure 2.4. Analysis of porosity of each column by imaged section. Time evolution is suppressed in this representation.

Column S1 should show only dissolution effects. As shown in Fig. 2.3, the porosity of column S1 increased from 32% to 36% after the first column flow period. Subsequent to that the data suggests the porosity remained roughly the same after two more shorter periods of exposure to STWL flow at 45°C. We do not have imaged data for S1 after exposure to flow at 89°C. Fig. 2.4 also shows the variation in porosity measurements taken on each of the two measured sections of column S1. Since the measurements are taken over time, the mean and standard deviation measurements plotted are time-averaged.

Column S3 should show combined quartz dissolution and cancrinite precipitation effects. Initially (Fig. 2.3) the porosity of the column sections is seen to increase (from 32% to 34%), but after exposure to STWL at 89°C, the porosity drops (to 30%).

2.2 A New Throat Finding Algorithm – Throats Cross!

Initial analysis of the pore network structure on columns S1, S3 and S4 using the throat finding algorithms in the 3DMA-Rock softeware consistently resulted in the appearance of a single large pore occupying an extreme portion (~40%) of the total pore space in most images. During the final third period of this project we have identified the source of the problem: *we have discovered that throat surfaces intersect each other.* While the occurance of such intersections is small for (consolidated) materials with porosity less than 20% (or in special cases of high-porosity media if the pores are very regular in shape), for geologic media exceeding 20% porosity, especially unconsolidated material, the occurance of throat intersections grows rapidly (in column S3 we estimate that 28% of all throat surfaces intersect with another).

Fig. 2.5 illustrates throat intersection with an artificial example. The pores labeled 1 and 2 are separated by a throat; so are pores 2 and 3; 3 and 4; and 4 and 1. These throats border one another (intersect).
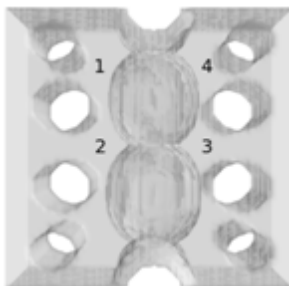
Figure 2.5. An artificial porous medium consisting of a back and front plate joined by 8 solid cylinders, four on the left, four on the right. For representation purposes, the insides of the solid cylinders are not shown – only the cylinder surface. The sample has top and bottom plates. A "column" of two solid spheres "welded" to each other are also "welded" to half-sphere indentations on the bottom and top plates. These two spheres do not contact the front and back plates. The sample is open on the left and right sides. There is void space between the plates, cylinders and spheres. The numbered regions indicate the positions of 4 of the interior pores.
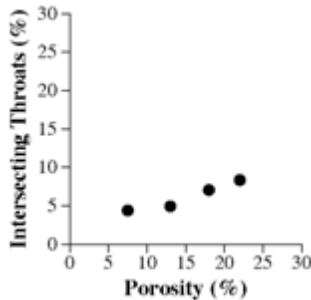
Fig. 2.6 displays the result of an LSMPQS[1] simulation of drainage (wetting angle = 0°) through this network. The (planar) throat surfaces (black) can clearly be seen to intersect each other. The

snapshots of the flow clearly show how throat surfaces, intersecting each other at 90°, act as capillary barriers simultaneously in each of the two directions.

To our knowledge, none of the extant throat finding algorithms account for the possibility that throat surfaces can intersect. Lack of such accounting in the existing algorithmns in 3DMA-Rock resulted in many throats being missed and produced the observed "large pore" behavior. We have therefore developed a new throat finding algorithm[2] which explicitly accounts for intersecting throats. (The throats shown in Fig. 2.6 were computed using the new algorithm.) For considerations of speed and robustness, the new algorithm approximates throats as planar surfaces. (In Fig. 2.6, symmetry considerations show that the throats are, for this sample, indeed planar. In the general case, this will not be true.)

Figure 2.6. LSMPQS simulation of drainage flow (top to bottom) through the network of Fig. 2.5. The non-wetting fluid is dark grey; the wetting fluid is light grey. The computed planar throat surfaces are black. There are 32 throats, 9 on the left side, 9 on the right and 14 running through the middle.

Figure 2.7. Observed increase in the frequency of intersecting throats (expressed as a percentage of all throats) with porosity.

We have tested our new algorithm on a well studied set of Fontainebleau samples[3] of porosity 7.5% to 22 % as well as column S3 (32.5% porosity). Fig. 2.7 plots the percentage of all throats that intersect as a function of porosity of the investigated sample. Over the porosity range 7.5% to 22%, the percentage of intersecting throats increased at the rate of 0.31% per percent porosity change. Over the porosity range 22% to 32.5% intersecting throats increased at the significantly greater rate of 1.81% per percent porosity change, indicating the need for throat finding algorithms that capture intersecting throats. For column S3, 27.95% of all throats intersect with another.

In Fig. 2.8 we compare the results of the new throat finding algorithm ("PD") against the previous throat finding algorithm[4] ("PLS") used in 3DM-Rock on the Fontainbleau samples as well as on column S3. Fig. 2.10 compares throat area and pore volume distributions. Throat finding consists of two major phases, identifying throats followed by constructing a pore-throat network. Some modification of the identified throats takes place occurs during the network construction phase. For the PD algorithm this consists of splitting throats and eliminating some spurious large area throats. For the PLS algorithm, this consists of deleting any throat that separates more than two pores. Throat area distributions are therefore compared at the end of

[1] Prodanovic, M. and S. L. Bryant. 2006. *J. Colloid Interf. Sci.,* 304:442-458

[2] Kim, J., D. Kim,, and W.B. Lindquist. 2013. Submitted to *Water Resourc. Res.*

[3] Lindquist, W. B., A. Venkatarangan, J. Dunsmuir, and T. F. Wong. 2000. *J. Geophys. Res.,* 105:21509-21527

[4] Prodanovic, M., W. B. Lindquist, and R. S. Seright. 2006. *J. Colloid Interf. Sci.,* 298:282-297

each of these two phases. For the lower porosity Fontainbleau samples, while the overall shape of the area distributions is similar at the end of the first phase, the PLS distribution is shifted slightly to larger area. At the end of the network construction phase, there is a marked difference in the distribution of smaller throat sizes due to the splitting of blocking (intersecting) throats in the PD algorithm. Such throats are discarded in the network construction phase of the PLS algorithm. The pore volume distributions, available after the pore-network construction phase, are very similar between the two algorithms.
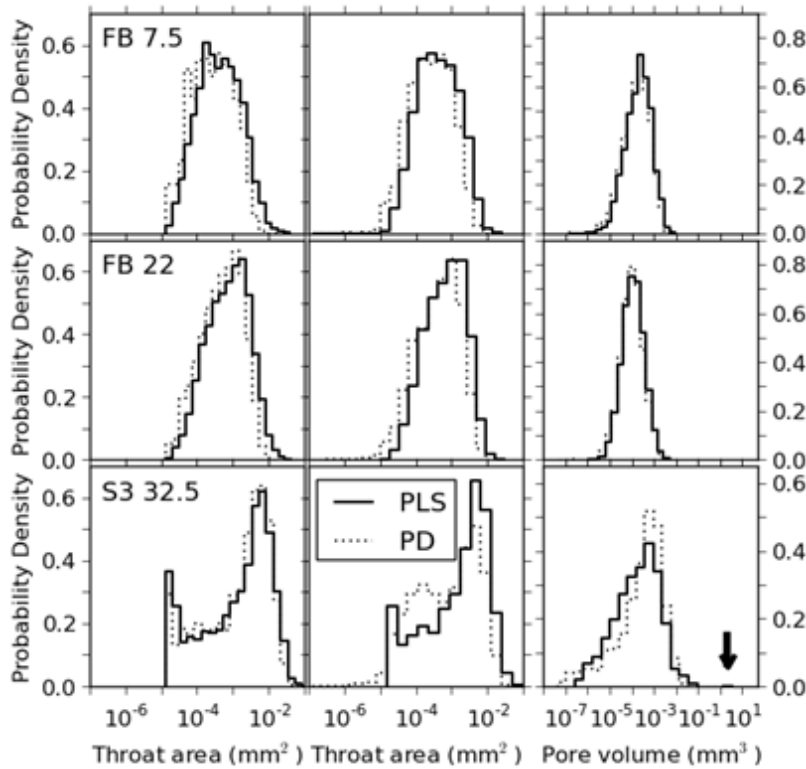
Figure 2.8. Throat area and pore volume distributions for the 7.5% and 22% porosity Fontainebleau sandstone images(first and second rows) and column S3 image(third row) using the new PD algorithm compared to the results of the PLS algorithm. The left throat area graph is the distribution of throats which algorithms are found and the center throat area graph is that of throats which are used at the pore-throat network.

For column S3, the throat distributions after the throat identification phase are similar for the two algorithms, but the PLS algorithm finds 11% fewer throats. After pore-network construction, the significant proportion of intersecting throats located (and retained) by the PD algorithm results in marked differences between the throat area distributions. Rejection of the possibility of intersecting throats by the PLS algorithm has drastic consequences in pore partitioning. The pore-network construction from the PLS algorithm resulted in a largest pore having volume 2.03 mm^3. In contrast, the largest pore constructed by the PD algorithm had a volume of 0.03 mm^3. The pore volume distributions show more distinct differences than the lower porosity Fontainebleau comparisons.

The production of large pores by the PLS algorithm in high porosity samples is the most significant consequence of neglecting intersecting throats. Such pores have very large coordination number.

2.3 Pore Network Analysis

We have computed pore volume and throat size distributions to investigate the effects of the dissolution and precipitation processes on the pore network. Fig. 2.9 displays these distributions. We examine the distributions for S4 first. There is little change in the distributions with time consistent with a sealed column for which reactions are essentially quenched. For column S1 which experiences only quartz dissolution, one would expect a uniform increase in pore volumes – that is a translation of the distribution to larger volumes, with a similar behavior in throat area distributions. This is not at all evident in the results for S1 – rather we see a more complex evolution of the distributions at small and
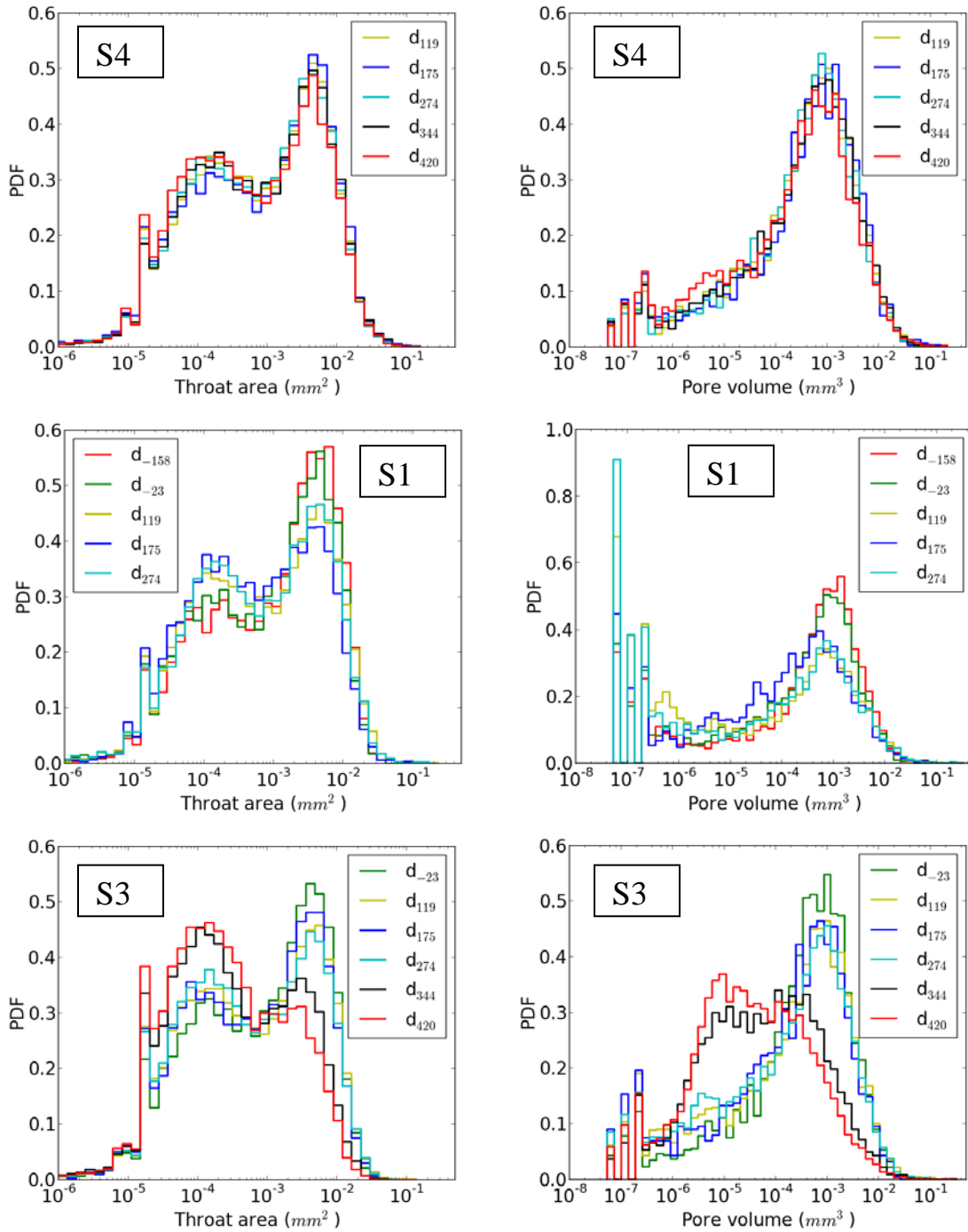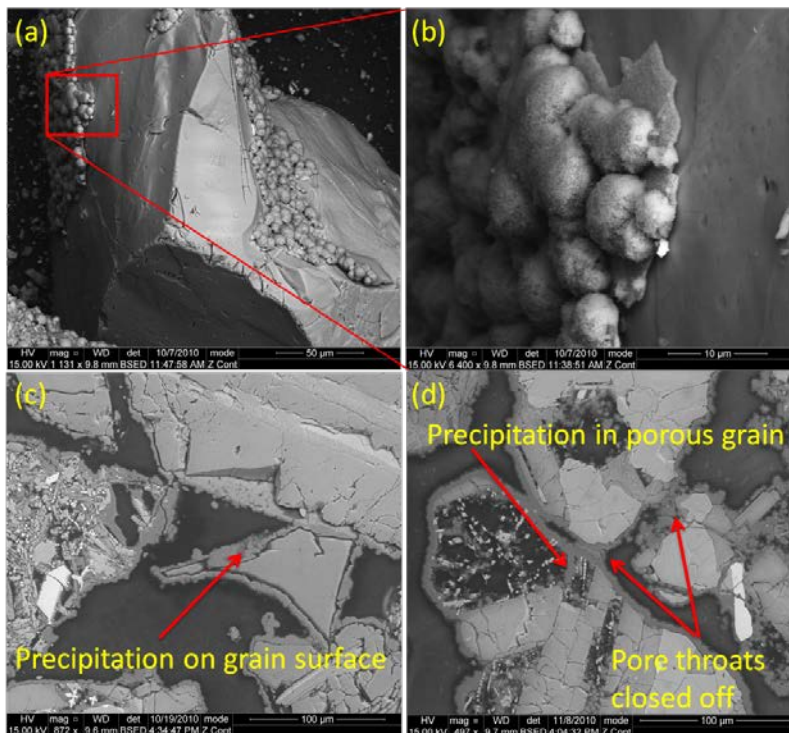
Figure 2.9. Throat area and pore volume distributions (averaged over all sections) as a function of time for the three columns analyzed in this study.

intermediate size ranges. *We believe what we are seeing is consistent with grain settling as dissolution occurs.* This illustrates a feature of dissolution processes in unconsolidated media that wil be (more) suppressed in consolidated media. For column S3, the cancrinite precipitation accompanying quartz dissolution serves to limit grain movement. As a consequence we see radical growth in the number of pores with volumes between 10^{-6} and 10^{-3} mm[3], and in the number of

throats with area between 10^{-5} and 10^{-2} mm^2. it appears that there is a decrease in the number of pores with volume exceeding 10^{-3} mm^3 and in the number of throats with area exceeding 10^{-2} mm^2. This is merely a consequence of displaying probability density functions (PDFs) in Fig. 2.9 (whose area is always unity), which emaphasizes relative weighting of the different parts of the density. In fact, the number of large size throats and pores remains essentially unchanged.

2.4 2D SEM Imaging of Reacted Columns

2D image analysis work at Princeton focused on analysis of Column X to examine reaction-induced changes in pore structure. Column X filled with 200-300 µm Hanford sand and reacted with simulated tank waste at PNNL. Before reaction, and periodically during, the column had been sent to Brookhaven National Lab to be imaged using 3D XCMT imaging at the Synchrotron National Light Source[5]. After the final XCMT analysis, Column X was shipped to Princeton for 2D Scanning Electron Microscopy (SEM) analysis. The column was impregnated with epoxy, sectioned, and imaged using the FEI Quanta FEG Environmental SEM in Princeton's Imaging and Analysis Center. Column cross-sections were analyzed to determine pore and throat size distributions with sodalite/cancrinite precipitation present and with precipitation digitally removed.


This work was published in L.E. Crandell, C.A. Peters, W. Um, K.W. Jones, W.B. Lindquist, 2012. "Changes in the pore network structure of Hanford sediment after reaction with caustic tank wastes." *Journal of Contaminant Hydrology* 131 (2012) 89–99. In brief, two morphologies of secondary mineral precipitates were revealed and it was found that these precipitates may not be chemically bonded to the grain surface (Figure 2.10). Secondary cancrinite precipitates were found as a relatively uniform coating on all grain surfaces. To determine how mineral

Figure 2.10. SEM images of (a and b) sodalite/cancrinite precipitation on loose reacted Hanford sand grain surfaces and (c and d) polished Column X cross-sections.

precipitates altered the pore network structure, cross-sectional images were stitched together to cover an area of 7.5 mm^2. A pre-precipitation scenario was created using a novel procedure for digitally removing mineral matter identified as secondary precipitates (Figure 2.12). Porosity was found to be up to 0.11 less after reaction. Erosion-dilation analysis was used to compute pore and throat size distributions (Figure 2.11). To correct for the inherent bias in the 2D analysis, a method was developed to bias-correct the size distributions. Precipitation decreased throat sizes and the abundance of large throats. These findings agree with previous findings based on 3D X-ray CMT imaging,

---

[5] Cai, R., W.B. Lindquist, W. Um, and K.W. Jones. 2009. *Adv. Water Resources,* 32:1396-1403

observing decreased porosity, clogging of small throats, and little change in large throats. However, 2D imaging found an increase in small pores, mainly in intragranular regions or below the resolution of the 3D images. Also, an increase in large pores observed via 3D imaging was not observed in the 2D analysis. Changes in flow conducting throats that are the key permeability-controlling features were observed in both methods.
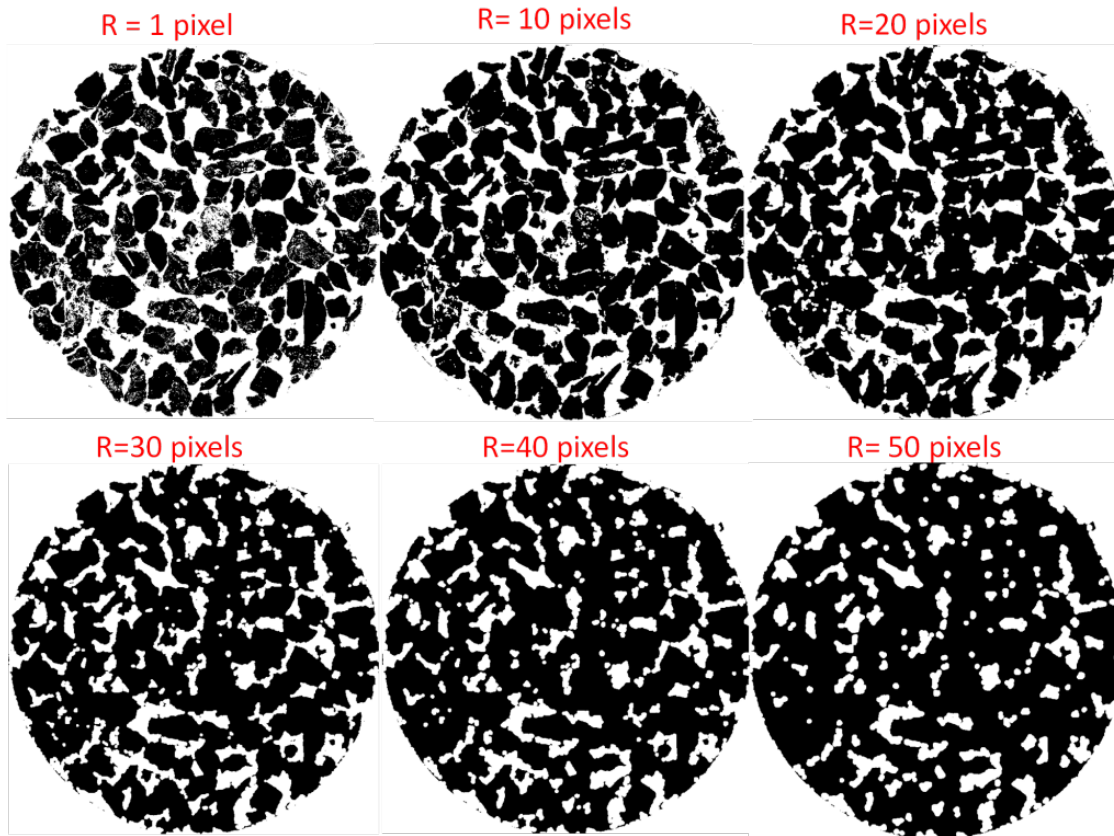
Figure 2.11: Cross section showing evolution of pore space using erosion-dilation analysis as size of structuring element increases from 1 to 50 pixels.
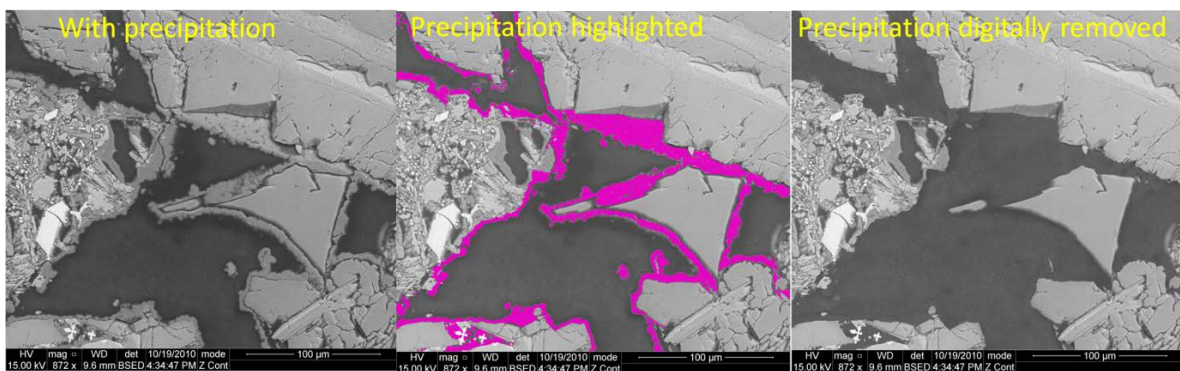
Figure 2.12: SEM images from cross section of Column X shown with precipitation and progression to version with precipitation digitally removed.

2D SEM imaging also revealed Hanford sand grains have a large amount of intragranular porosity and that secondary mineral precipitates were observed in this intragranular space. This observation suggests radionuclides will be sequestered in intragranular regions, which may decrease their mobility

in migrating water. However, as the systm recovers and uncontaminated pore water contacts the reacted sediments, secondary contamination will occur as the radionuclides desorb from soils. To examine this, the long-term leaching of Cs from intragranular pores in contaminated sediments was estimated. Two reactive transport model scenarios were investigated, one accounting for Cs sorption in intragranular pores and one that includes only sorption to surfaces in contact with the bulk pore fluid. These models reveal that Cs leaching is slow and requires 105 to 591 days to desorb all exchangeable Cs from a soil segment. In addition, Cs sorbed to soil downstream will not desorb until the depletion of upstream exchangeable Cs. Intragranular pores will prolong the period of secondary contamination at the site, as desorption of Cs sorbed in intragranular pores will not begin until the depletion of Cs sorbed to the bulk soil, further elongating the time to begin downstream Cs desorption.

3. Multi-Scale Modeling and Up-Scaling

3.1 2D and 3D imaging resolution trade-offs in quantifying pore throats for prediction of permeability

Although the impact of subsurface geochemical reactions on porosity is relatively well understood, changes in permeability remain difficult to estimate. In this work, pore-network modeling was used to estimate permeability based on pore- and pore-throat size distributions determined from 2D Scanning Electron Microscopy (SEM) images of thin sections and 3D X-ray computed microtomography (CMT) images. Figure 3.1 depicts a conceptualization of the two methods for informing the pore network model. The analyzed specimens were a Viking sandstone sample from the Alberta sedimentary basin and an experimental column of reacted Hanford sediments.

For Column X, a decrease in permeability due to mineral precipitation was estimated, but the permeability estimates were found to be dependent on imaging technique and resolution. X-ray CT imaging has the advantage of reconstructing a 3D pore network while 2D SEM imaging can easily analyze sub-grain and intragranular variations in mineralogy. Pore network models informed by analyses of 2D and 3D images at comparable resolutions produced permeability estimates with relatively good agreement. Large discrepancies in predicted permeabilities resulted from small variations in image resolution. Images with resolutions 0.4 to 4 μm predicted permeabilities differing by orders of magnitude. While lower-resolution scans can analyze larger specimens, small pore throats may be missed due to resolution limitations, which in turn overestimates permeability in a pore-network model in which pore-to-pore conductances are statistically assigned. Conversely, high-resolution scans are capable of capturing small pore throats, but if they are not actually flow-conducting predicted permeabilities will be below expected values. In addition, permeability is underestimated due to misinterpreting surface-roughness features as small pore throats. Comparison of permeability predictions with expected and measured permeability values showed that the largest discrepancies resulted from the highest resolution images and the best predictions of permeability will result from images between 2 to 4 μm resolution. To reduce permeability underestimation from analyses of high-resolution images, a resolution threshold between 3 and 15 μm was found to be effective, but it is not known whether this range is applicable beyond the samples studied here.
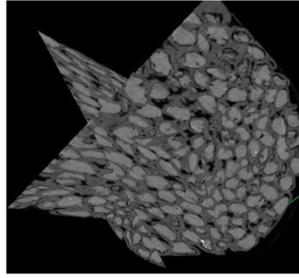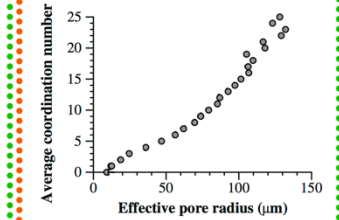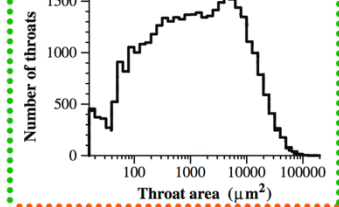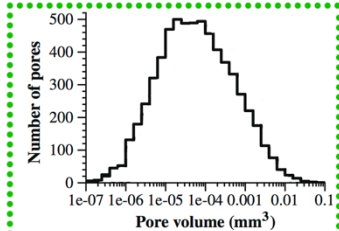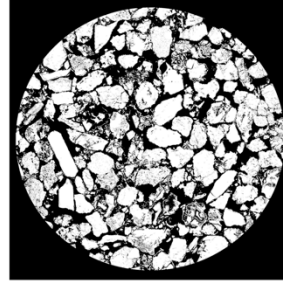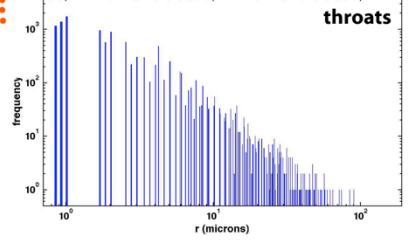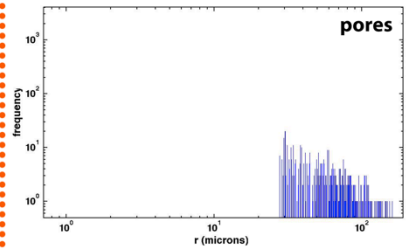
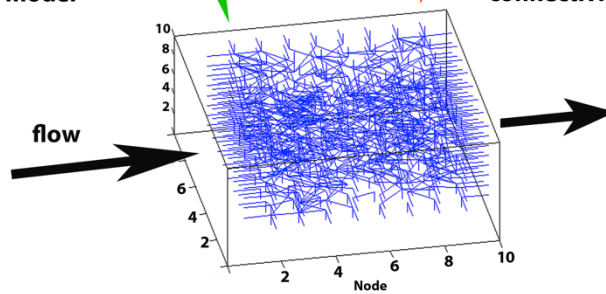**Figure 3.1.** Conceptualization of the process of informing pore-network models withinformation from 3D X-ray CMT or 2D SEM imaging.

3.2 Permeability evolution due to dissolution and precipitation of carbonates using reactive transport modeling in pore networks

Modeling reactive transport in porous media offers an insight on how geochemistry and the transport of aqueous species influence upscaled parameters, such as porosity and permeability. In our study we are trying to understand - through pore-network modeling - how carbonate rocks in contact with CO_2-rich brines change due to the precipitation or dissolution of fast-reacting minerals such as calcite and dolomite. By better understanding the effects of these interactions we can make inferences on the effects that the injection of CO_2 for sequestration purposes might have on a sealing caprock, for example. The modeling at the pore scale is able to capture the fine scale pore-to-pore heterogeneity that dictates much of the ionic concentration distribution. We have chosen to model certain reactions and the transport of species at the pore-scale (as oppose to the continuum scale) because of the importance of accurately representing the spatial and time scales at which the kinetic and equilibrium reactions are valid.

A reactive transport model was developed to simulate reaction of carbonates (Table 3.1) within a pore network for the high-pressure CO_2-acidified conditions relevant to geological carbon sequestration. The pore network was based on a synthetic oolithic dolostone (Figure 3.2).

Table 3.1. Chemical reactions and equilibrium constants at 50 ^{o}C. The equilibrium values are from the EQ3/6 database [Wolery et. al, 1990].

|	Reactions	logK$_{eq}$
Equilibrium	$H_2O \leftrightharpoons OH^- + H^+$	-13.3
	$H_2CO_3^* \leftrightharpoons HCO_3^- + H^+$	-6.15
	$HCO_3^- \leftrightharpoons CO_3^{2-} + H^+$	-10.3
	$H_4SiO_4 \leftrightharpoons H_3SiO_4^- + H^+$	-9.83
	$H_3SiO_4^- \leftrightharpoons H_2SiO_4^{2-} + H^+$	-12.6
	$Al^{3+} + OH^- \leftrightharpoons Al(OH)^{2+}$	8.76
	$Al(OH)^{2+} + OH^- \leftrightharpoons Al(OH)_2^+$	18.9
	$Al(OH)_2^+ + OH^- \leftrightharpoons Al(OH)_3$	27.3
	$Al(OH)_3 + OH^- \leftrightharpoons Al(OH)_4^-$	33.2
	$CaCO_{3(s)} \leftrightharpoons Ca^{2+} + CO_3^{2-}$	-8.66
Kinetic	$CaAl_2Si_2O_{8(s)} + 8H^+ \leftrightharpoons Ca^{2+} + 2Al^{3+} + 2H_4SiO_4$	21.7
	$Al_2Si_2O_5(OH)_{4(s)} + 6H^+ \leftrightharpoons 2Al^{3+} + 2H_4SiO_4 + H_2O$	3.80
	$NaAlSi_3O_{8(s)} + 8H_2O \leftrightharpoons Na^+ + Al(OH)_4^- + 3H_4SiO_4$	-1.67
	$CaMg(CO_3)_{2(s)} + 2H^+ \leftrightharpoons Ca^{2+} + 2HCO_3^- + Mg^{2+}$	1.63
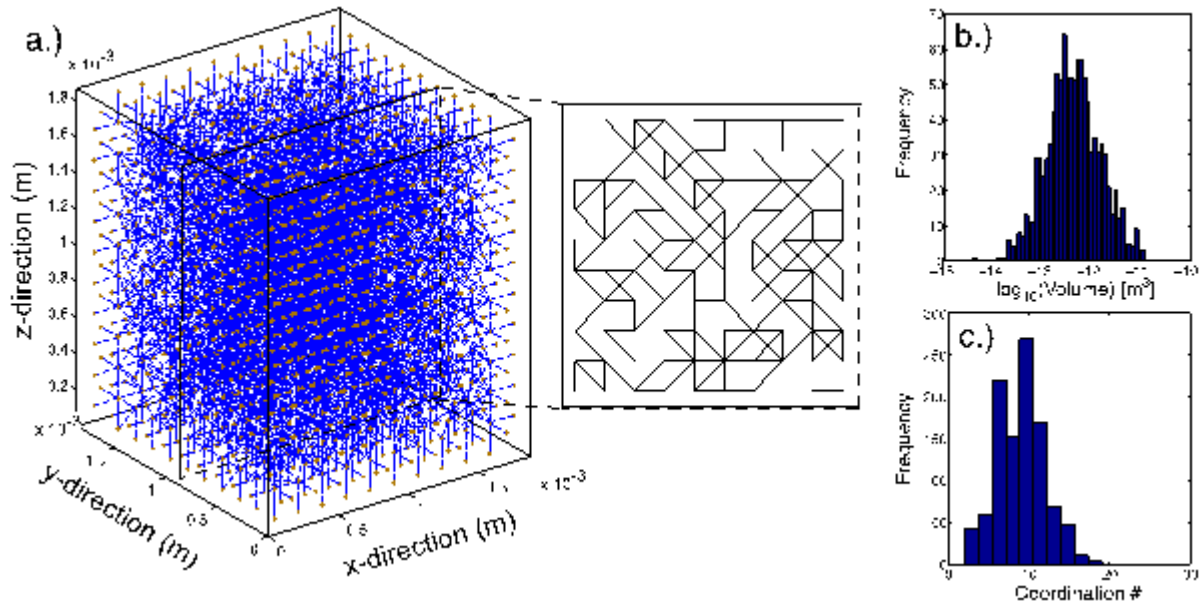
Figure 3.2. a.) Ball and stick representation of the network with a cross-sectional slice of the pore-to-pore connectivity. b.) Histogram of network pore volumes. c.) Histogram of network coordination numbers.

Simulation results produced insights that can inform continuum-scale models regarding reaction-induced changes in permeability and porosity. As expected, permeability was shown to increase extensively with dissolution caused by high concentrations of carbonic acid, but neither pH nor calcite saturation alone was a good predictor of the effects. Complex temporal evolutions of interstitial brine chemistry and network structure led to the counterintuitive finding that a far-from-equilibrium solution produced less permeability change than a nearer-to-equilibrium solution at the same pH. This was explained by the pH buffering that increased carbonate ion concentration and inhibited further reaction. Simulations of different flow conditions produced a non-unique set of permeability-porosity relationships. Diffusive-dominated systems caused dissolution to be localized near the inlet, leading to substantial porosity change but relatively small permeability change. For the same extent of porosity change caused from advective transport, the domain changed uniformly, leading to a large permeability change. Regarding precipitation, permeability changes happen much slower compared to dissolution-induced changes and small amounts of precipitation, even if located only near the inlet, can lead to large changes in permeability. Exponent values for a power law that relates changes in permeability and porosity ranged from 2 to 10, but a value of 6 held constant when conditions led to uniform changes throughout the domain.

Appendix A

R0 · R1 · R2

R3 · R4
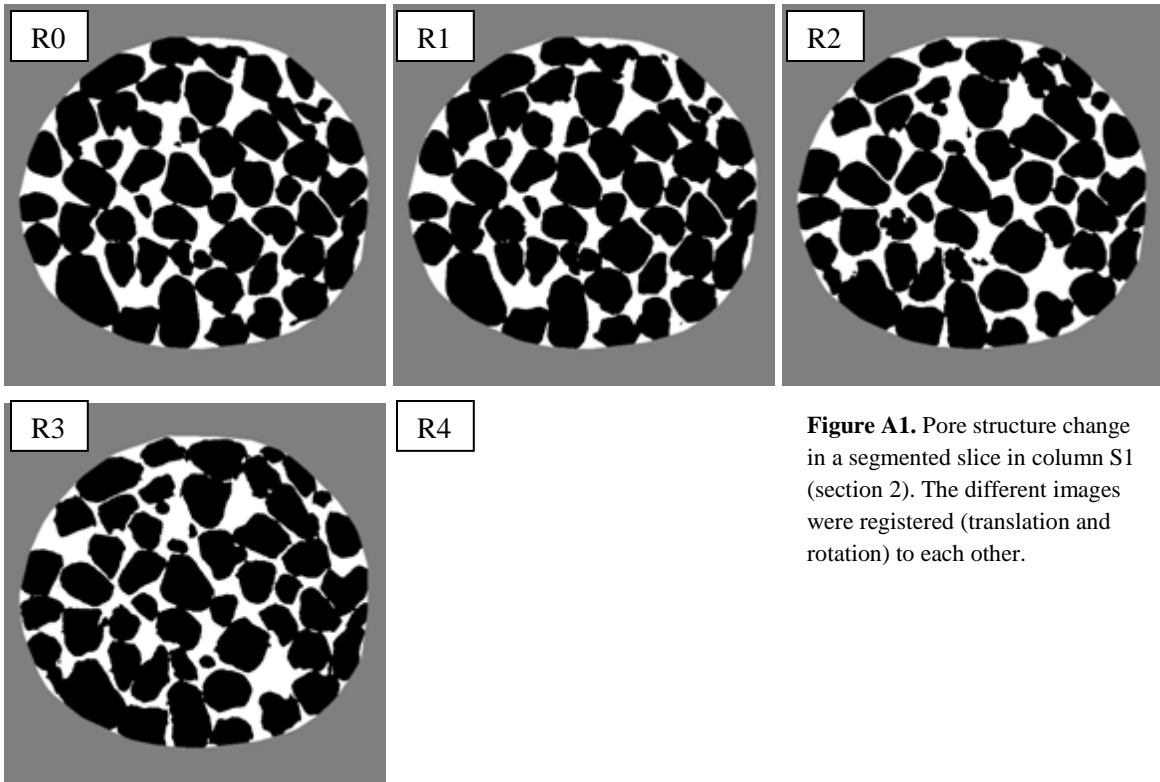
Figure A1. Pore structure change in a segmented slice in column S1 (section 2). The different images were registered (translation and rotation) to each other.

R1 · R2
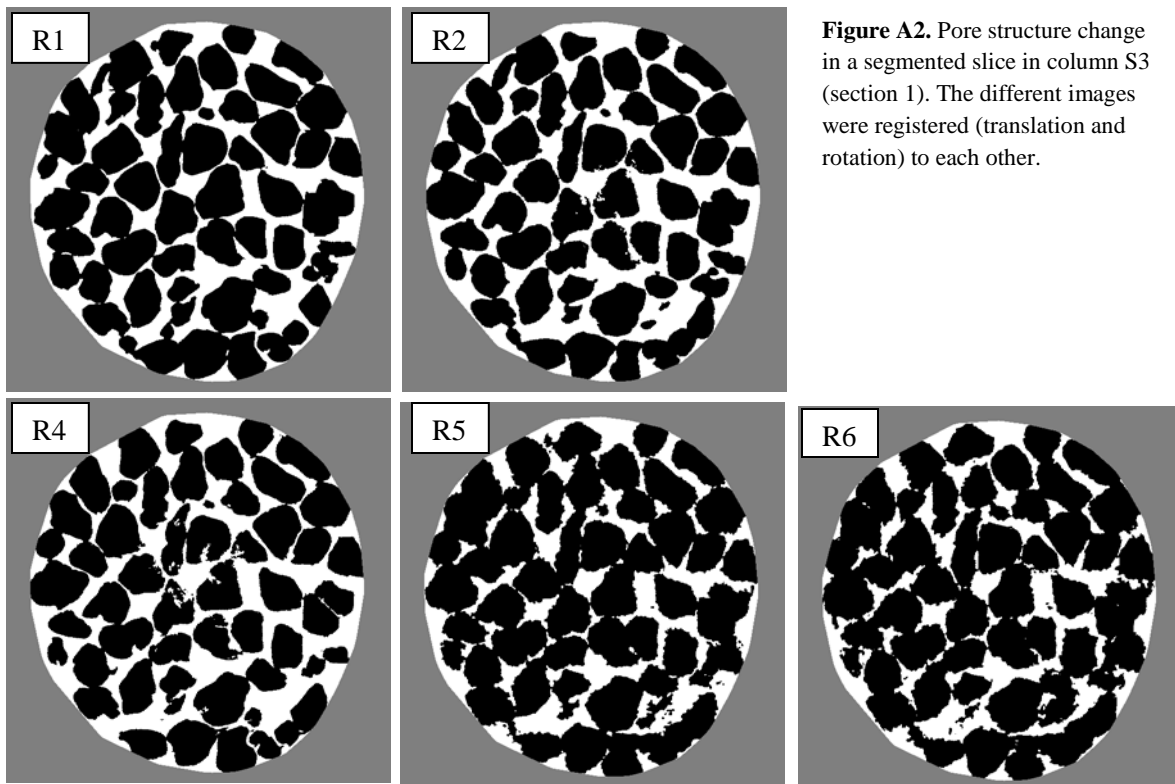
Figure A2. Pore structure change in a segmented slice in column S3 (section 1). The different images were registered (translation and rotation) to each other.

R4 · R5 · R6

Figure A3. Pore structure change in a segmented slice in column S4 (section 4). The different images were registered (translation and rotation) to each other.